PHYSICAL REVIEW B **93**, 054203 (2016)

Measurements of structural and chemical order in $Zr_{80}Pt_{20}$ and $Zr_{77}Rh_{23}$ liquids

M. L. Johnson,[1,*] M. E. Blodgett,[1] K. A. Lokshin,[2,3] N. A. Mauro,[4] J. Neuefeind,[5] C. Pueblo,[1] D. G. Quirinale,[6] A. J. Vogt,[7]
T. Egami,[2,3,8,9] A. I. Goldman,[6] and K. F. Kelton[1]
[1]*Department of Physics and Institute of Materials Science and Engineering, Washington University,*
St. Louis, Missouri, 63130, USA
[2]*Department of Materials Science and Engineering, University of Tennessee, Knoxville, Tennessee 37996, USA*
[3]*Joint Institute for Neutron Sciences, University of Tennessee and Oak Ridge National Laboratory, Oak Ridge, Tennessee 37831, USA*
[4]*Department of Physics, North Central College, Naperville, Illinois 60540, USA*
[5]*Chemical and Engineering Materials Division, Oak Ridge National Laboratory, Oak Ridge, Tennessee 37831, USA*
[6]*Department of Physics and Astronomy, Iowa State University, Ames, Iowa 50011, USA*
[7]*Instrument and Source Division, Oak Ridge National Laboratory, Oak Ridge, Tennessee 37831, USA*
[8]*Department of Physics and Astronomy, University of Tennessee, Knoxville, Tennessee 37996, USA*
[9]*Materials Science and Technology Division, Oak Ridge National Laboratory, Oak Ridge, Tennessee 37831, USA*

(Received 11 November 2015; revised manuscript received 11 January 2016; published 3 February 2016)

The short-range order (SRO) and medium-range order of electrostatically levitated $Zr_{80}Pt_{20}$ and $Zr_{77}Rh_{23}$ liquids are presented based on a combination of high-energy x-ray diffraction and time-of-flight neutron diffraction studies. The atomic structures of the $Zr_{80}Pt_{20}$ liquids were determined as a function of temperature from constrained reverse Monte Carlo simulations using x-ray and elastic neutron scattering measurements and two partial pair-distribution functions obtained from molecular dynamics (MD) simulations. Analysis of both the Faber-Ziman and Bhatia-Thornton partial structure factors shows that the $Zr_{80}Pt_{20}$ and $Zr_{77}Rh_{23}$ liquids have similar topological SRO. Interestingly, the chemical SRO appears to be much more strongly tied to the topological order in the $Zr_{77}Rh_{23}$ liquid than in the $Zr_{80}Pt_{20}$. These results demonstrate that the combination of experimental scattering measurements with MD results provides a powerful approach for obtaining details of chemical and topological ordering in metallic glasses and liquids.

DOI: 10.1103/PhysRevB.93.054203

I. INTRODUCTION

Although lacking long-range order, metallic liquids do have short-range order (SRO) and medium-range order (MRO), which have been intensely studied in recent years, both experimentally [1–11] and from simulations [12–14]. The SRO and MRO are important for understanding the nucleation and growth of crystalline phases [15] and can provide insight into metastable phase and glass formation. Frank first predicted that icosahedral SRO (ISRO), a highly coordinated structure that is incompatible with translational periodicity, is dominant in metallic liquids [16], providing a nucleation barrier for crystallization. Molecular dynamics (MD) simulations of liquids provide evidence that this is the case [17–19], and it has been observed experimentally in levitated elemental and alloy metallic liquids [11,20,21]. In one case, this order catalyzed the nucleation of a metastable icosahedral quasicrystal phase (i-phase) [15], confirming Frank's hypothesis of the role of ISRO on the nucleation barrier. Rapidly quenched Zr-rich compositions of Zr-Pt and Zr-Pd liquids are also known to form the i-phase [22–24], suggesting that the structures of these liquids could also be dominated by icosahedral order. Supporting this, amorphous Zr-Pt can be produced by rapid quenching if the oxygen concentration is increased [25], with the i-phase as the primary devitrification product [26,27] followed by the formation of the equilibrium hexagonal Zr_5Pt_3 phase [28]. Small changes in Pt concentration (from 20 at.% Pt to 27 at.% Pt) change the transformation behavior, with Zr_5Pt_3 becoming the primary devitrification product [29], bypassing the formation of the i-phase. Whereas other similar binary alloys, such as Zr-Rh, do not directly form the i-phase, additions of Rh to Zr-Cu binary alloys does lead to i-phase formation [30].

Previous x-ray scattering studies of Zr-Pt glasses have shown a prepeak at small q in the total structure factor, $S(q)$, suggesting a significant amount of chemically driven MRO in the amorphous structure [28,31,32]. Those studies indicate large amounts of icosahedral and distorted icosahedral SRO in the glass, with the prepeak arising from Pt-Pt correlations. X-ray scattering studies of supercooled $Zr_{80}Pt_{20}$ liquids suggest that this MRO begins in the high-temperature liquid and persists in the quenched glass [33]. A prepeak is also a common feature of Zr-[noble metal (NM)] eutectic liquids, such as Zr-Ir/Pt/Au [4]. However, whereas the NMs are all similar in size and have similar bonding strengths with Zr, x-ray scattering measurements of Zr-Rh and Zr-Pd eutectic liquids do not show a prepeak. Since the Faber-Ziman (FZ) weighting factors [34] scale with the square of the atomic number Z, the lack of a prepeak in Zr-Rh and Zr-Pd has been attributed to the small value of the solute-solute FZ coefficients compared with those for the other two partials [4] (Rh and Pd have smaller values of Z than Ir, Pt, and Au). It is of interest to further investigate this explanation and the reasons for glass and complex crystal phase formation in these alloys through more detailed structural studies.

Here, we report the results of combined wide-angle high-energy x-ray diffraction and time-of-flight (TOF) elastic neutron scattering studies on electrostatically levitated $Zr_{80}Pt_{20}$ and $Zr_{77}Rh_{23}$ liquids. An analysis of the data suggests that

---

[*] mjohnson@physics.wustl.edu

the lack of a prepeak is not simply due to the ratios of the FZ coefficients. Whereas the topological SRO is similar for both alloys, $Zr_{77}Rh_{23}$ has more prominent chemical SRO. Further, based on a Voronoi tessellation analysis of the atomic structure obtained from a reverse Monte Carlo (RMC) simulation of a $Zr_{80}Pt_{20}$ liquid that is constrained by the results of MD simulations, the liquid contains dominant polyhedra that are consistent with structural features of the equilibrium Zr_5Pt_3 crystalline phase. Due to the topological similarity between $Zr_{77}Rh_{23}$ and $Zr_{80}Pt_{20}$, a new phase is predicted, Zr_5Rh_3 (Mn_5Si_3 type), which is found as a metastable primary crystallizing phase in the deeply supercooled $Zr_{77}Rh_{23}$ liquid. Whereas the free energies of the stable crystal phases are lower, the similarity in structure to that of the liquid decreases the nucleation barrier, thus favoring the formation of the metastable phase.

II. EXPERIMENT

Master ingots for all compositions were prepared by arc-melting high-purity Zr (99.95 at.%, which contained Hf to a nominal concentration of 3 at.%), Pt (99.95 at.%), and Rh (99.8 at.%) on a Cu hearth in a high-purity (99.999 at.%) Ar atmosphere. A Ti-Zr getter located close to the sample was melted prior to arc-melting the master ingots to further reduce the oxygen concentration in the chamber. The master ingots were melted three times to ensure that the samples were homogeneous; each melt cycle lasted approximately 1 min. Mass loss during arc-melting was negligible (less than 0.1%). The master ingots were subsequently crushed, and portions were remelted to obtain small spherical samples (∼2.5 mm diameter) that were processed in a containerless environment using the Washington University Beamline Electrostatic Levitation (WU-BESL) facility [35,36]. The WU-BESL is optimized for x-ray diffraction studies of levitated, containerlessly processed liquids in a high-vacuum environment ($\sim 10^{-7}$ Torr). It was used for *in situ* structural studies of the levitated liquids at the Advanced Photon Source (APS) at sector 6-ID-D. Additional master ingots were crushed and remelted into slightly larger spherical samples (∼3 mm diameter, 100 mg) for *in situ* elastic neutron scattering studies of the levitated liquids at the Spallation Neutron Source (SNS) located at Oak Ridge National Laboratory (ORNL). These studies were made on the Nanoscale-Ordered Materials Diffractometer (NOMAD) beamline [37] using the Neutron Electrostatic Levitator (NESL) [38–40]. The NESL is optimized for TOF elastic and inelastic neutron studies of levitated liquid samples in a vacuum environment; the pressure at the sample location was $\sim 8 \times 10^{-7}$ Torr for these studies.

A. X-ray scattering details

For the x-ray experiments, the liquid samples were heated, melted, and subsequently thermally processed using a fiber-coupled diode laser (980 nm, 50 W continuous maximum power output). Crystallization of the supercooled liquid, marked by a sharp rise in temperature (recalescence), limited the lowest accessible temperature for the x-ray diffraction studies to 190 °C below the liquidus temperature (T_L). A Process Sensors Metis MQ22 two-color ratio pyrometer, operating at 1.40 and 1.65 μm wavelengths, was used for high-temperature measurements ($600-2300\,^{\circ}$C) of the liquids. A constant emissivity ratio was assumed for the entire temperature range over which structural data were acquired. The emissivity ratio was calibrated by matching the onset of the melt plateau (corresponding to the solidus temperature T_S in the temperature versus time curve measured on heating in WU-BESL) to the largest endothermic signature measured in a differential thermal analyzer (DTA; Labsys DTA/DSC, Setaram) [41].

The temperature was correlated with noncontact measurements of the volume, made using the shadow method [42,43] with a PixeLINK PL-B74IG CMOS camera and a 455 nm collimated microscope light-emitting diode (LED). The relative precision of the density data was ∼0.3% over the temperature range studied, with an absolute accuracy of ∼0.5%; the measurement error is dominated by errors in the calibrations of the volume and mass. A more detailed discussion of the machine vision volume measurement algorithm and experimental implementation can be found elsewhere [42,44].

The x-ray diffraction studies of the liquids were made in a transmission geometry using high-energy x-rays ($E = 130$ keV, $\lambda = 0.0956$ Å for $Zr_{80}Pt_{20}$, $E = 132$ keV, $\lambda = 0.094\,03$ Å for $Zr_{77}Rh_{23}$). Scattering data were obtained to a maximum momentum transfer q of 20 Å^{-1} at a sampling rate of 1 Hz using a GE Revolution 41-RT amorphous Si flat-panel x-ray detector. The sample-to-detector distance, detector tilt, and detector center were calibrated by fitting the diffraction pattern of a levitated polycrystalline Si sample. These values were confirmed using a NIST Si standard in a capillary placed at the position of the levitated liquid sample. The scattering data obtained were processed by masking bad pixels, applying a pixel efficiency gain map, averaging the images obtained during the isothermal hold, and subtracting the appropriate detector dark current and scattering background. Images were then corrected for oblique incidence, absorption, multiple scattering, fluorescence, polarization, sample geometry, and Compton scattering contributions using in-house analysis packages written in LabVIEW [45]. A series of measurements were made at each temperature step (15–20 s) to obtain the total static structure factor using

$$S(q) = \frac{I(q) - \sum_{i=1}^{n} c_i |f_i(q)|^2}{\left|\sum_{i=1}^{n} c_i f_i(q)\right|^2} + 1, \qquad (1)$$

where $I(q)$ is the measured diffraction intensity, c_i is the atomic fraction of each elemental species, and $f_i(q)$ is the q-dependent atomic form factor for each species. The sums were taken over all species, and an isotropic and statistically homogeneous atomic distribution was assumed. The total pair-distribution function $g(r)$ and the reduced pair-distribution function $G(r)$ were computed from a Fourier transform of the structure factor using

$$\begin{aligned} G(r) &= 4\pi \rho_{\rm exp} r(g(r) - 1) \\ &= \frac{2}{\pi} \int q(S(q) - 1) \sin(qr)\, dq, \end{aligned} \qquad (2)$$

where $\rho_{\rm exp}$ is the average number density calculated from the experimentally determined volume and mass.

B. Neutron scattering details

For the neutron experiments, the liquid samples were heated, melted, and subsequently thermally processed using a pair of fiber-coupled diode lasers (980 nm, 110 W continuous maximum power output) positioned on opposite sides of the sample. Two lasers were used to ensure even heating and to minimize the temperature gradient across the larger samples. Temperatures of the levitated NESL samples were measured from 500 to 1800 °C using a single Process Sensors Metis MQ22 two-color ratio pyrometer. A constant emissivity ratio was assumed for the entire temperature range over which structural data were acquired. The emissivity ratio was calibrated in a similar manner as the WU-BESL measurements [41]. Due to long timescale drift in the positioning lasers, the sample slowly shifted relative to the pyrometer, causing an apparent temperature drift in the sample. The melt plateau was measured before and after each measurement in order to calibrate the isothermal temperature.

The TOF elastic neutron diffraction studies of the electrostatically levitated liquids were made using high-energy neutrons ($E = 10\,\mathrm{meV}$–$10\,\mathrm{eV}$, $\lambda = 0.1$–$2.9\,\mathrm{\AA}$). Scattering data were obtained to a maximum momentum transfer of $100\,\mathrm{\AA}^{-1}$ for a series of isothermal measurements (30–60 min). Diamond powder contained in a vanadium can located in the approximate sample position was used to calibrate the sample-to-detector distances for each ^{3}He linear position sensitive detector covering a scattering angle 2θ of 3–175°. A levitated sample of incoherently scattering vanadium was used to measure the incident distribution of neutron energies for subsequent normalization once coherent Bragg peaks were removed. Both the sample and vanadium measurements were corrected with an empty chamber scan. Absorption and multiple scattering contributions were simulated for both the sample and vanadium measurements based on a spherical sample geometry using the measured sample mass and density and were removed from the scattering data [37].

The $S(q)$s obtained from the neutron scattering experiments contained a large curvature, causing poor normalization around unity. This feature corresponds to inelastic scattering contributions that are manifest as large unphysical peaks in the small-r region of $G(r)$ ($r < 1$ Å). These oscillations were replaced with a linear fit to the hard-sphere region where it is expected that $G(r) = -4\pi\rho r$. The difference between the experimental ripples and the fit was then Fourier transformed back into q space and subtracted from the initial $S(q)$. This method produces physically realistic behavior in the hard-sphere region and removes inelastic scattering contributions below the first nearest-neighbor distance, removing the curvature in $S(q)$ [46].

In order to effectively compare two independently measured structure factors, they must both appear on the same absolute scale. Incomplete accounting for secondary scattering, i.e. neutrons scattered by the sample that undergo subsequent scattering from the environment before being detected, is one of the primary causes of incorrect scaling. In practice, it is nearly impossible to properly model the secondary scattering without knowing the precise location and material composition of each part of the sample environment. However, some approximations can be made from the expected physical behavior. The Peterson metric [47], ΔG_{low} [Eq. (3)], quantifies the magnitude of ripples in $G(r)$ below some cutoff before the first peak r_{low}, which corresponds to the hard-sphere cutoff where no atom may be located

$$\Delta G_{\mathrm{low}} = \frac{\int_0^{r_{\mathrm{low}}} \left[rG(r) + 4\pi r^2 \rho_{\mathrm{fit}}\right]^2 dr}{\int_0^{r_{\mathrm{low}}} \left(4\pi r^2 \rho_{\mathrm{fit}}\right)^2 dr}. \tag{3}$$

The parameter ρ_{fit} is the number density calculated from the slope of a linear fit to $G(r)$ below r_{low}. The slope of this region was adjusted to minimize ΔG_{low}, minimizing the deviation from linear behavior. The measured $S(q)$ was then multiplied by a scaling factor α according to the method described by Peterson *et al.* [47] using

$$S'(q) = \alpha S(q) + (1 - \alpha). \tag{4}$$

Here, $S'(q)$ is the corrected structure factor and the additive constant of $(1 - \alpha)$ is required to maintain oscillation of the structure factor about unity. Since α is a constant, it propagates through a Fourier transform and changes the scaling in real space as well, without otherwise changing or distorting the real space features. It was adjusted until the experimentally measured number density ρ_{exp} matched ρ_{fit}. This treatment was applied to the $S(q)$s obtained from both the x-ray and neutron measurements and was confirmed to give identical results for measurements of identical alloys at the same temperature from two separate x-ray scattering studies.

C. RMC fits

Atomic configurations were obtained from the scattering data with the RMC technique [48] using RMC_POT [49]. By constraining the fits with the results from the x-ray and neutron scattering experiments, physically reasonable, chemically specific partial structure factors (PSFs) could be obtained. In addition, fits to the liquid $\mathrm{Zr_{80}Pt_{20}}$ data were constrained using the Zr-Zr and Zr-Pt partial pair-distribution functions (PPDFs) obtained from *ab initio* MD simulations [33]. The starting configurations for the RMC fits contained 10000 atoms (8000 Zr, 2000 Pt) that were randomly distributed in a cubic box of a size constrained by $\rho_{\mathrm{exp}}(T)$, as measured using WU-BESL. Minimum PPDF cutoff distances were used to improve the convergence time; these were set at 2.2, 2.2, and 2.4 Å for Zr-Zr, Zr-Pt, and Pt-Pt, respectively. The atomic configurations obtained from the RMC fits were analyzed with Voronoi tessellation techniques [50,51] using Voro++ [52]. Recently, the importance of weighted bisectors in the Voronoi analysis has become clear [53]. The effect of weighted bisectors is to create a larger separation in the average coordination numbers (CNs) of the large and small atoms by more accurately modeling how much space each individual atom encompasses. The elemental Goldschmidt radii [54] were used to calculate more physically realistic bisecting planes between two atoms of different sizes. Because the liquid structure is already disordered and the local CN is continuously changing, the time-averaged atomic configuration will contain many unphysically sized faces that incorrectly identify an atom as a neighbor. To correct for this effect, faces with an area smaller than $0.25\,\mathrm{\AA}^2$ were removed. This cutoff was determined from the maximum face area that caused a histogram of edge sizes to appear to follow a Gaussian distribution without altering the shape of the large-edge size. The constrained reverse Monte Carlo (CRMC) fits were performed eight times for each temperature to generate sufficient statistics and determine the error bars in the Voronoi analysis.

III. RESULTS AND DISCUSSION

A. Liquid x-ray and neutron scattering measurements

The total structure factors $S(q)$ were measured for $Zr_{80}Pt_{20}$ and $Zr_{77}Rh_{23}$ liquids from high-energy x-ray and TOF neutron scattering data obtained over a temperature range of $980-1300\,^{\circ}\mathrm{C}$ (Fig. 1). While the oscillations in $S(q)$ damp to close to unity by $q = 12\,\text{Å}^{-1}$ in liquids, the NOMAD instrument can acquire high-quality data to much larger q (Fig. 2). As the temperature of $Zr_{80}Pt_{20}$ is decreased below the solidus temperature ($T_S = 1177\,^{\circ}\mathrm{C}$, measured with DTA) into the supercooled liquid, the primary peak sharpens, and the second peak develops a distinct shoulder. These features indicate that the liquid structure is becoming increasingly ordered as preferred length scales emerge during cooling. Due to the limited temperature range over which $Zr_{77}Rh_{23}$ was measured ($\Delta T = 50\,^{\circ}\mathrm{C}$), very little peak evolution was observed. For both alloys, the primary peak from x-ray scattering data is shifted to slightly larger q than in the neutron scattering experiments; the shift is more noticeable in the broad second peak. These features are due to differences in the weighting of the PSFs between the x-ray and neutron scattering, likely revealing chemically specific short-range ordering (CSRO).

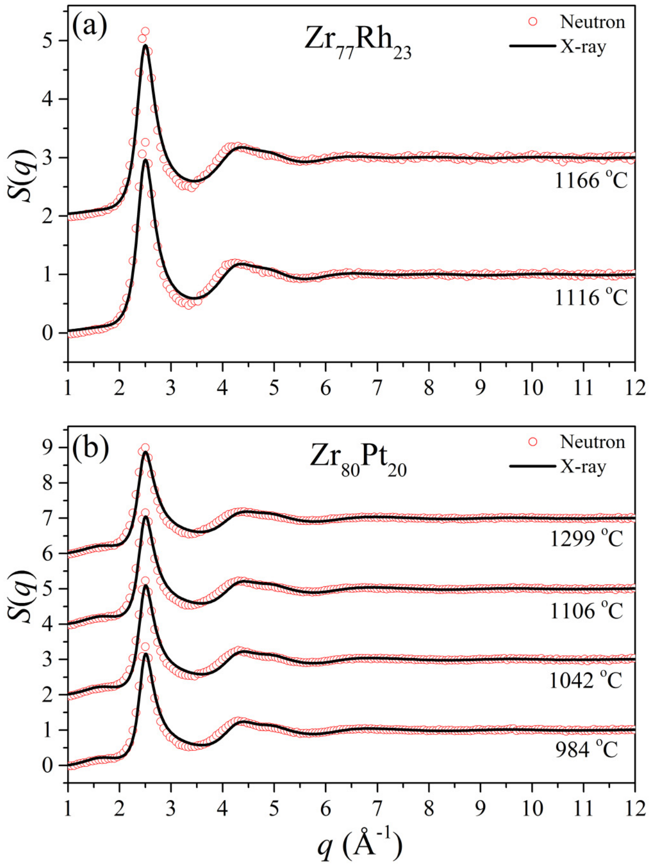

FIG. 1. Total $S(q)$s measured for levitated liquid (a) $Zr_{77}Rh_{23}$ and (b) $Zr_{80}Pt_{20}$ using both x-ray (solid black line) and neutron (open red circles) scattering. Each temperature is vertically offset by 2 for clarity.

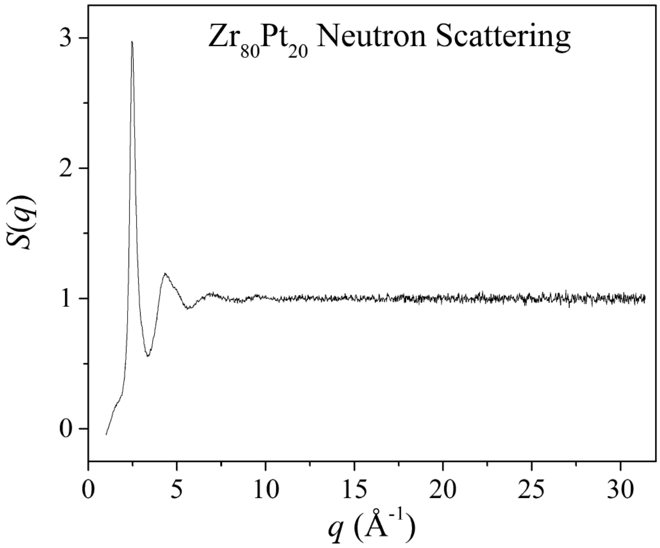

FIG. 2. Example $S(q)$ for $Zr_{80}Pt_{20}$ at $1293\,^{\circ}\mathrm{C}$ out to $32\,\text{Å}^{-1}$ showing the range of the NOMAD instrument.

The $S(q)$ for $Zr_{80}Pt_{20}$ contains a prepeak at $q \sim 1.6\,\text{Å}^{-1}$, consistent with previous liquid [4,33] and glass studies [28,31,55]. Appearing in both x-ray and neutron data, it is greatly reduced in the latter (Fig. 3). This feature has been argued to reflect the Pt-Pt correlation between Pt-centered icosahedronlike clusters [31,33,56]. It is interesting to note that, while many of the features of the $Zr_{77}Rh_{23}$ and $Zr_{80}Pt_{20}$ $S(q)$s are remarkably similar, the prepeak is absent in the $S(q)$s obtained from both x-ray and neutron scattering studies of liquid $Zr_{77}Rh_{23}$. A previous study of the MRO in Zr-(NM) liquids [4] suggested that the same type of chemical order is likely present in all of these alloy liquids, but that the prepeak

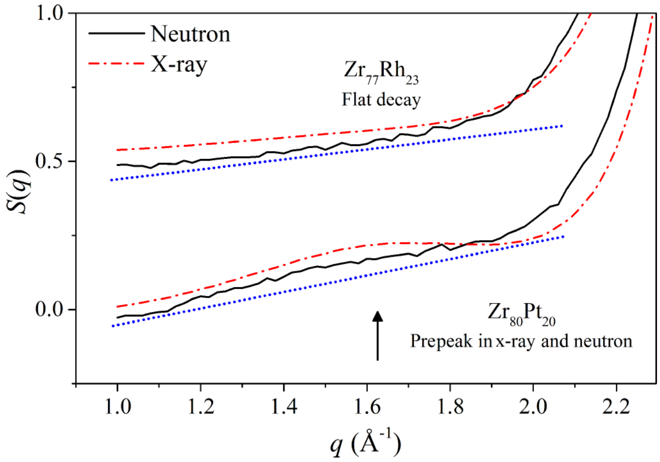

FIG. 3. Neutron (solid black line) and x-ray (dashed-dotted red line) scattering in the low-q region at $\sim 1110\,^{\circ}\mathrm{C}$ for $Zr_{77}Rh_{23}$ (top) and $Zr_{80}Pt_{20}$ (bottom) liquids (vertically offset by 0.5 for clarity). The dotted blue lines are guides to the eye to emphasize the prepeak that appears in $Zr_{80}Pt_{20}$ from neutron scattering.

TABLE I. Measured liquid density and change with temperature [see Eq. (6)]. T_S was obtained from DTA.

Composition	T_S(°C)	ρ_S (g cm^{-3})	$d\rho/dT$ (g cm^{-3} °C^{-1})
$Zr_{80}Pt_{20}$	1177 ± 5	8.38 ± 0.01	$-3.30 \pm 0.02 \times 10^{-4}$
$Zr_{77}Rh_{23}$	1061 ± 5	7.22 ± 0.01	$-3.24 \pm 0.02 \times 10^{-4}$

might not appear due to smaller chemical contrast from the FZ [34] weighting factors.

The relative amplitudes of the first coordination shell features can be described within the FZ formalism [34], where the PPDFs ($g_{ij}(r)$) are related to the PSFs ($S_{ij}(q)$) by

$$g_{ij}(r) - 1 = \frac{1}{4\pi\rho_{\text{exp}}}\frac{1}{\pi}\int (S_{ij}(q)-1)\frac{\sin(qr)}{qr}q^2dq. \quad (5)$$

Here, ρ_{exp} is the experimentally measured number density (Table I) and is given by

$$\rho_{\text{exp}}(T) = \rho_S + \frac{d\rho}{dT}(T - T_S). \quad (6)$$

Here, T_S is the solidus temperature measured from DTA and ρ_S is the liquid number density measured at T_S. For x-ray scattering, the total $g(r)$ is related to the partials using the q-dependent FZ weighting factor w_{ij}, where, as $q \to 0$,

$$w_{ij}(0) = c_i c_j \frac{Z_i Z_j}{\langle Z\rangle^2}. \quad (7)$$

Here, c_i is the concentration of the ith atomic species, and Z_i is the number of electrons in each species. For neutron scattering, Z is replaced by the neutron scattering length b. When the features in the PSFs vary rapidly with q compared to the atomic form factors, the total pair-correlation function can be approximated as a simple q-independent weighted sum of the partial pair-correlation functions

$$g(r) \cong \sum_i \sum_j w_{ij}(0) g_{ij}(r). \quad (8)$$

This approximation is valid for amorphous metallic alloys and is discussed in more detail elsewhere [2,57–59]. For neutrons, b is independent of q and Eq. (8) becomes exact. The calculated x-ray weighting factors for $Zr_{77}Rh_{23}$, $w_{ij}^{X,\text{ZrRh}}$, are almost equal to the neutron weighting factors for $Zr_{80}Pt_{20}$, $w_{ij}^{N,\text{ZrPt}}$ (Table II). By the argument given previously [4], since no prepeak is observed in x-ray measurements for $Zr_{77}Rh_{23}$, it should not be observable in the neutron scattering data for $Zr_{80}Pt_{20}$. That it is observed, however, indicates that the two liquids must have different topological and/or chemical ordering, calling into question the previous interpretation of similar structures among Zr-NM liquids [4].

TABLE II. FZ weighting factors for x-ray and neutron scattering [see Eq. (7)].

Alloy	Scattering type	w_{ii}	w_{ij}	w_{jj}
$Zr_{80}Pt_{20}$	X-ray	0.451 95	0.440 65	0.107 41
	Neutron	0.560 93	0.376 04	0.063 02
$Zr_{77}Rh_{23}$	X-ray	0.560 22	0.376 51	0.063 26
	Neutron	0.643 97	0.317 01	0.039 01

B. Constrained RMC

As discussed in Sec. II C, atomic configurations for the $Zr_{80}Pt_{20}$ liquid were generated from the experimental scattering data using the RMC technique [48]. It is important to note that, while producing realistic results, RMC structures are not unique. They are the most disordered structures that can describe the experimental data. Since the measured $S(q)$s are already averaged over many liquid configurations due to the rapid dynamics in the liquid and the long acquisition times, the structures obtained from RMC are reasonable approximations to this average. However, while the total structure factor is generally well reproduced, RMC structures obtained from a single experimental x-ray or neutron scattering constraint do not properly capture chemical order, yielding unphysical PPDFs. This can be improved by constraining the RMC fits with multiple experimental inputs, such as from x-ray, neutron, and extended x-ray absorption fine structure (EXAFS) measurements, as well as with PPDFs obtained from MD simulations.

The RMCs were constrained using experimental $S(q)$s obtained from x-ray and neutron scattering measurements, $S^{\text{X}}(q)$ and $S^{\text{N}}(q)$, of $Zr_{80}Pt_{20}$. Since two experimental measurements are not sufficient to resolve the chemical partials in a binary alloy, MD partials were used as additional constraints. In order to generate an atomic configuration that most closely represented experimental measurements, the number of simulated constraints was minimized. Since the original MD simulation contained only 20 Pt atoms [33], the Pt-Pt MD partial likely contains large statistical variations. Thus, the simulations were additionally constrained using only the Zr-Zr and Zr-Pt partials from MD. The $S(q)$s from the CRMCs agreed well with both x-ray and neutron measurements [Fig. 4(a)], although several features were less consistent with the neutron measurements. Good agreement was also found in $g(r)$, although there were some discrepancies in the amplitude and position of the first peak compared with those obtained from the neutron scattering studies [Fig. 4(b)]. If the CRMC was performed using only the Zr-Pt partial from MD as an additional constraint, much better agreement was found between experiment and the CRMC, suggesting that the potential used in the MD simulations may be misrepresenting the interaction between Zr atoms.

When compared with the PPDFs obtained from MD, both $g_{\text{ZrZr}}(r)$ and $g_{\text{ZrPt}}(r)$ were well reproduced. This is not surprising since they were input constraints to the CRMC fit [Figs. 5(a)–5(b)]. The most significant difference with MD was in $g_{\text{PtPt}}(r)$ [Fig. 5(c)], where the very small first peak grew in amplitude and shifted to slightly larger r. This is consistent with previous CRMC results made using EXAFS measurements of $Zr_{80}Pt_{20}$ glasses [60]. The amplitude of the second-neighbor shell ($r \sim 4.5$ Å) for $g_{\text{PtPt}}(r)$ is also increased. The higher-order peaks are not consistent with the MD results. These differences suggest that the small number of Pt atoms in the MD simulation cannot fully represent the medium-range and extended ordering.

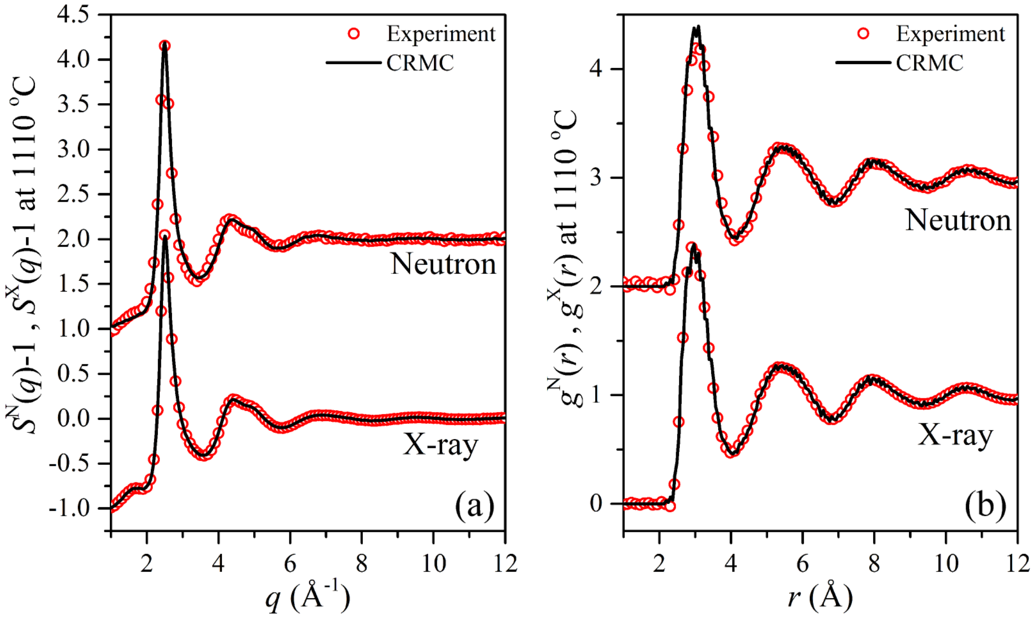

FIG. 4. Results of CRMC (solid black line) fits to experimental (open red circles) results for $Zr_{80}Pt_{20}$ liquid at 1110 °C for (a) $S(q)-1$ and (b) $g(r)$ for both neutron (top curves) and x-ray (bottom curves) scattering (the neutron results are offset by 2 for clarity).

The PSFs from the CRMC were in very good agreement with the Zr-Zr and Zr-Pt MD partials [Figs. 6(a)–6(b)], as expected. The largest differences are again for the Pt-Pt partial [Fig. 6(c)]. As argued previously, the prepeak in $S(q)$ near $q = 1.6\,\text{Å}^{-1}$ is due to Pt-Pt correlations beyond those of nearest neighbors. This is consistent with the large feature around 4.5 Å in $g_{\text{PtPt}}(r)$ [Fig. 5(c)] and the large peak around $1.6\,\text{Å}^{-1}$ in $S_{\text{PtPt}}(q)$ [Fig. 6(c)]. The peak in g_{PtPt} at $r \sim 4.5\,\text{Å}$ is significantly reduced if the prepeak is masked in S_{PtPt}, suggesting that this is the dominant length scale for the medium-range Pt-Pt correlation. This is consistent with interatomic distances in different types of interpenetrating

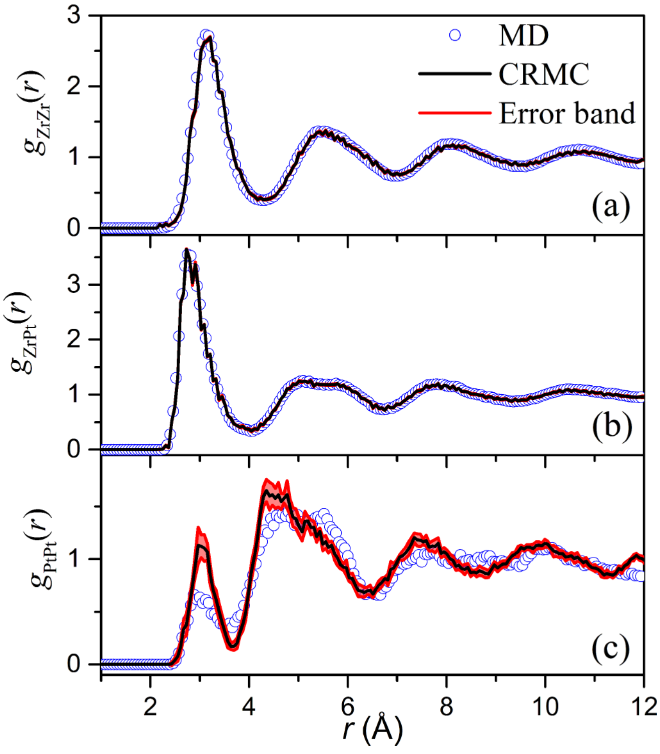

FIG. 5. Comparisons of the PPDFs from MD (open blue circles) and CRMC (solid black line) for (a) $g_{\text{ZrZr}}(r)$, (b) $g_{\text{ZrPt}}(r)$, and (c) $g_{\text{PtPt}}(r)$. The largest differences were observed with $g_{\text{PtPt}}(r)$.

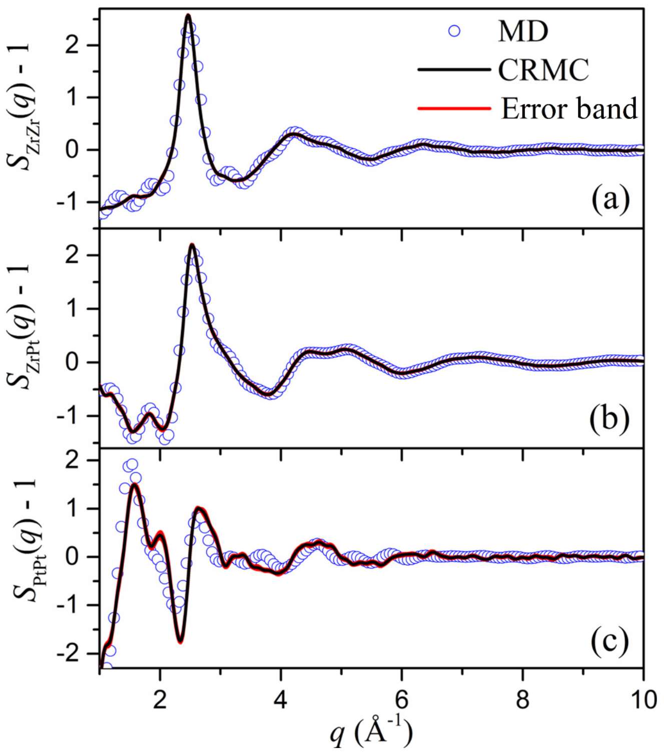

FIG. 6. Comparisons of the PSFs from MD (open blue circles) and CRMC (solid black line) for (a) $S_{\text{ZrZr}}(q)$, (b) $S_{\text{ZrPt}}(q)$, and (c) $S_{\text{PtPt}}(q)$. The largest differences were observed with $S_{\text{PtPt}}(q)$.

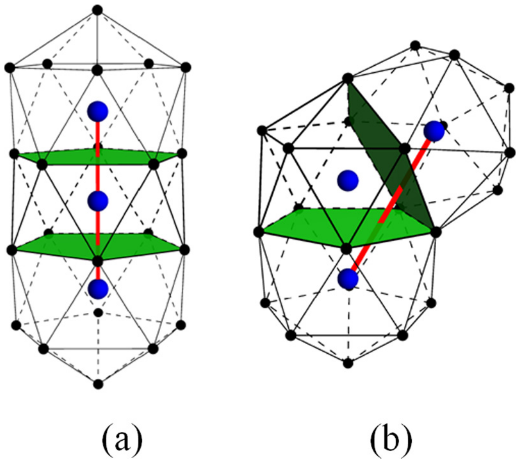

FIG. 7. (a) Capped and (b) diagonal interpenetrating icosahedra. The center of each icosahedron is represented by a blue sphere. A red line connects the centers of neighboring interpenetrating icosahedra.

Pt-centered icosahedra [31,56]. The approximate distances between the center Pt atoms for these clusters are 4.55–5 Å in a capped configuration [Fig. 7(a)] and 4–4.3 Å in a diagonal configuration [Fig. 7(b)]. In a highly disordered liquid containing a distribution of icosahedrallike clusters, these distances are likely smeared out, creating the broad peak in $g_{\mathrm{PtPt}}(r)$ centered at 4.5 Å.

C. Bhatia-Thornton partial structures

The total structure factor for a binary alloy can also be expressed within the Bhatia-Thornton formalism [61] [Eq. (9)]. This structure factor $S_{BT}(q)$ is described in terms of fluctuations in density [topological order, $S_{NN}(q)$], fluctuations in chemical concentration [chemical order, $S_{CC}(q)$], and the cross-correlation between topological and chemical order [$S_{NC}(q)$]:

$$S_{BT}^{N}(q) = \frac{\langle b\rangle^2}{\langle b^2\rangle} S_{NN}(q) + \frac{2\langle b\rangle(b_i - b_j)}{\langle b^2\rangle} S_{NC}(q) + \frac{(b_i - b_j)^2}{\langle b^2\rangle} S_{CC}(q). \tag{9}$$

Here, b corresponds to the neutron scattering length, and i,j correspond to the first and second elements in the binary alloy, respectively. $S_{CC}(q)$ is defined such that, at large q, it converges to $c_i c_j$. Although the order of $b_i - b_j$ is important for the interpretation of $S_{NC}(q)$, reversing the alloy equation only changes the sign. $S_{BT}(q)$ can be calculated for x-ray scattering by replacing b_i with the q-dependent atomic form factor $f_i(q)$, as is done within the FZ formalism. The BT PSFs can also be described in terms of the FZ partials using:

$$\begin{aligned}
&(a)\ \ S_{NN}(q) = c_i^2 S_{ii}(q) + 2c_i c_j S_{ij}(q) + c_j^2 S_{jj}(q)\\
&(b)\ \ S_{NC}(q) = c_i^2 c_j S_{ii}(q) + \left(c_i c_j^2 - c_i^2 c_j\right) S_{ij}(q) - c_i c_j^2 S_{jj}(q)\\
&(c)\ \ S_{CC}(q) = c_i^2 c_j^2 (S_{ii}(q) - 2S_{ij}(q) + S_{jj}(q)) + c_i c_j.
\end{aligned} \tag{10}$$

For $Zr_{80}Pt_{20}$, all three FZ partials were obtained from CRMC and converted to the BT formalism using Eq. (10) [Fig. 8(a)]. For $Zr_{77}Rh_{23}$, the weighting factor for $S_{CC}(q)$ in both x-ray and neutron scattering is negligible compared to $S_{NN}(q)$ and $S_{NC}(q)$ (between 1 and 2%), so Eq. (9) reduces to an equation with only two unknowns, $S_{NN}(q)$ and $S_{NC}(q)$, which can be uniquely determined with two experimental inputs. The equivalent PPDFs, $g_{NN}(r)$, $g_{NC}(r)$, and $g_{CC}(r)$, are then obtained from a Fourier transform of the PSFs [Fig. 8(b)]. Although the amplitude of the $Zr_{80}Pt_{20}$ $S_{NN}(q)$ partial is slightly larger than that of $Zr_{77}Rh_{23}$, $S_{NN}(q)$ is very similar in all other aspects. Topologically then, the ordering in the two liquids appears to be very similar, with similar correlation lengths present. This similarity is also evident in $g_{NN}(r)$, where again similar peak shapes and positions are found. When the CRMC is constrained by the two experimental measurements and only one additional MD partial (Zr-Pt), it is found that $g_{NN}(r)$ is nearly identical in $Zr_{77}Rh_{23}$ and $Zr_{80}Pt_{20}$ (Fig. 9). As noted earlier, this also results in better overall agreement between the CRMC and the experimental measurements. Since it is unclear why the Zr-Pt partial is consistent with the experimental measurements while the Zr-Zr partial is not, both were used as constraints for the CRMC results presented here. Perhaps the similarity in topological order between these alloys is not surprising since, in the limit of $c_j \to 0$, $S_{NN}(q)$ equals $S(q)$ for the pure element (Zr in this case) and Rh and Pt are of similar size ($r_{\mathrm{Pt}} = 1.38$ Å, $r_{\mathrm{Rh}} = 1.34$ Å) and in adjacent columns and rows on the periodic table. However, $S_{NN}(q)$ in another pair of alloy liquids where the solutes are again in adjacent columns in the periodic table ($Zr_{64}Ni_{36}$ and Zr_2Cu) show very different topological order [62]. This could be a consequence of the lower solute concentrations in the Zr-Pt and Zr-Rh liquids, with the order constrained by the Zr, or it simply indicates that it is possible for alloy liquids with similar atomic sizes to behave quite differently.

The positive peak in $S_{CC}(q)$ for $Zr_{80}Pt_{20}$ near 1.6 Å^{-1} [Fig. 8(a)] suggests that the prepeak in the total $S(q)$ arises from atoms of the same chemical species that are arranged in a regular pattern within the overall topology. Taken with the results of CRMC, this is consistent with a Pt-Pt correlation. There is also a corresponding positive peak in $g_{CC}(r)$ near 4.5 Å, consistent with the Pt-Pt correlation observed in the second coordination shell of $g_{\mathrm{PtPt}}(r)$.

The cross-correlation terms, $S_{NC}(q)$ and $g_{NC}(r)$, are often described as representing a "size effect." The negative peak in $g_{NC}(r)$ for $Zr_{80}Pt_{20}$ near 2.75 Å suggests there is a higher density of atoms surrounding Pt atoms at that distance than around Zr. The corresponding negative peak in $g_{CC}(r)$ suggests that atoms of opposite species tend to associate at this length scale, consistent with the high chemical affinity between Zr and Pt. Similarly, the positive peak near 3.2 Å suggests a larger density of atoms surrounding Zr atoms at that distance than around Pt atoms. These results are consistent with fewer atoms packing around the smaller Pt atoms than are around the larger Zr atoms. The lack of features in $g_{CC}(r)$ at $r = 3.2$ Å implies that there is no preference for Zr over Pt atoms at this length scale. The negative peak in $g_{NC}(r)$ near 4.5 Å again suggests a higher density of atoms around Pt atoms relative to around Zr, and the corresponding positive peak in $g_{CC}(r)$ is consistent with there being a preference for those atoms to also be Pt. This is consistent with the medium-range correlations previously discussed in the FZ formalism.

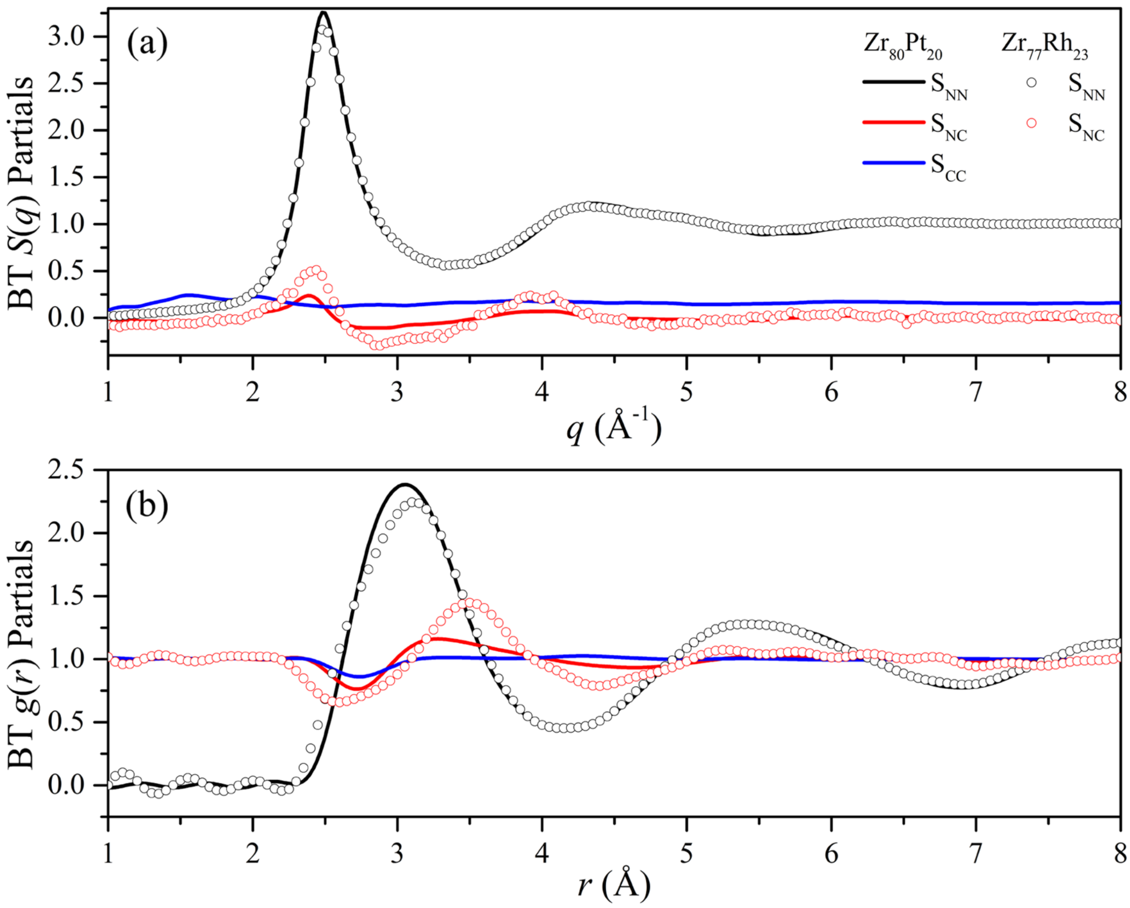

FIG. 8. (a) $S(q)$ and (b) $g(r)$ Bhatia-Thornton partials for $Zr_{80}Pt_{20}$ (solid lines) and $Zr_{77}Rh_{23}$ (open symbols) at 1106 °C. The topological order (NN) is similar between both alloys.

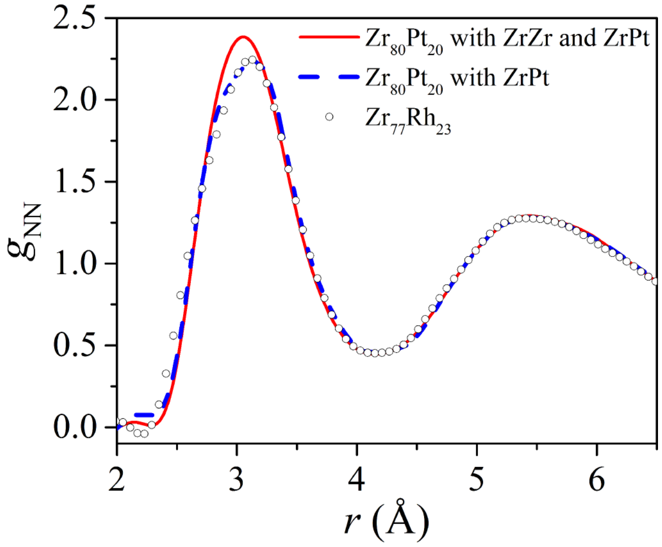

FIG. 9. Comparisons of $g_{NN}(r)$ between $Zr_{77}Rh_{23}$ (open gray circles) and $Zr_{80}Pt_{20}$ for different CRMC results. Similar topological order is found if $Zr_{80}Pt_{20}$ is constrained with both the Zr-Zr and Zr-Pt partials from MD (solid red line), but the agreement is much better if $Zr_{80}Pt_{20}$ is constrained with only Zr-Pt from MD (dashed blue line). In both cases, the simulations are additionally constrained with both x-ray and neutron measurements.

It is interesting to note that, while $Zr_{80}Pt_{20}$ and $Zr_{77}Rh_{23}$ are similar in their topological order, the size effect is much larger for $Zr_{77}Rh_{23}$, despite Pt and Rh having very similar atomic radii, and suggests that the chemical order in $Zr_{77}Rh_{23}$ is more strongly tied to the topological order than in $Zr_{80}Pt_{20}$. It seems that the stronger heat of mixing between Zr-Pt than between Zr-Rh should at least make up for this difference, if not surpass it. Without $g_{CC}(r)$ available for $Zr_{77}Rh_{23}$, it is impossible to know what chemical order overlays the topological configuration, but it is possible that Zr-Rh forgoes the establishment of medium-range correlations between Rh-atoms in favor of increased chemical SRO. This would explain the lack of prepeak in $S^X(q)$ for $Zr_{77}Rh_{23}$ while it exists in $S^N(q)$ for $Zr_{80}Pt_{20}$, despite their identical FZ weighting factors. The stronger heat of mixing of Zr-Pt compared to Zr-Rh most likely originates from larger charge transfer between Zr-Pt than Zr-Rh because the Fermi level of Pt is lower than Rh. Thus, the chemical MRO is enhanced in Zr-Pt because of Pt-Pt repulsion, whereas the size difference between Zr and Pt is reduced, making $S_{NC}(q)$ and $g_{NC}(r)$ smaller.

D. Voronoi tessellation

To further probe the liquid structures, the Voronoi tessellations were computed for the atomic configurations gen-

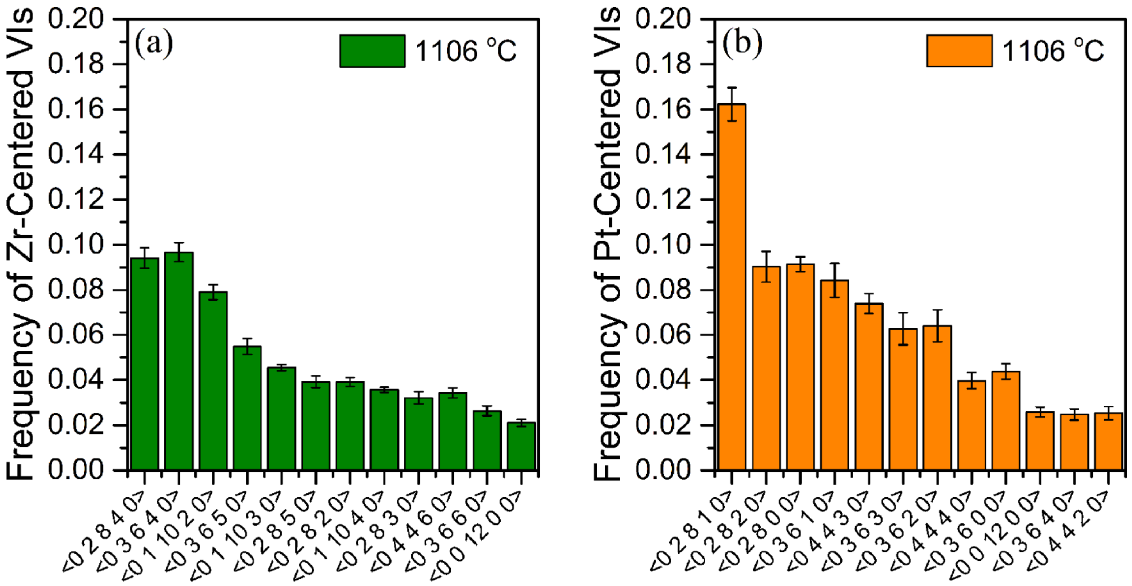

FIG. 10. Frequency of the dominant VIs at 1106 °C for (a) Zr-centered and (b) Pt-centered structures. Temperature dependent indices are provided in the Supplemental Material [65].

erated for $Zr_{80}Pt_{20}$ from CRMC. A broad distribution of Zr-centered clusters is found, with many indices appearing with a frequency greater than 2% [Fig. 10(a)]. The majority of these clusters are distorted, consistent with Frank-Kasper (FK) polyhedra [63] with large CNs (CN = 12–15). This suggests that the environment surrounding Zr atoms is heavily distorted. Within the statistical error generated for these Voronoi indices (VIs), there are no discernible trends with temperature. Three dominant clusters (frequency greater than 6%) were identified, corresponding to ⟨0 2 8 4 0⟩, ⟨0 3 6 4 0⟩, and ⟨0 1 10 2 0⟩, but none occurred with a frequency greater than 10%.

While no single VI constitutes more than 10% of the total of Zr-centered polyhedra, the Pt-centered clusters are dominated by ⟨0 2 8 1 0⟩, the CN = 11 FK polyhedron, with a frequency greater than 15% [Fig. 10(b)]. This polyhedron appears to be very stable; it was also shown to be dominant in the structures of $Zr_{80}Pt_{20}$ glasses [31,55]. It corresponds to the Pt-centered cluster in the Zr_5Pt_3 equilibrium crystal phase [64], which is also the second phase to devitrify from amorphous ribbons following the formation of the quasicrystal [28]. While the ⟨0 2 8 1 0⟩ cluster is clearly the most dominant, other polyhedra with CN = 10–12 also appear with frequencies between 2 and 9%. Interestingly, perfect icosahedra, ⟨0 0 12 0 0⟩, are only weakly present in the high-temperature liquids, but their frequency nearly doubles upon supercooling (see Supplemental Material [65]). The icosahedral-like clusters, ⟨0 2 8 2 0⟩ and ⟨0 3 6 3⟩, are

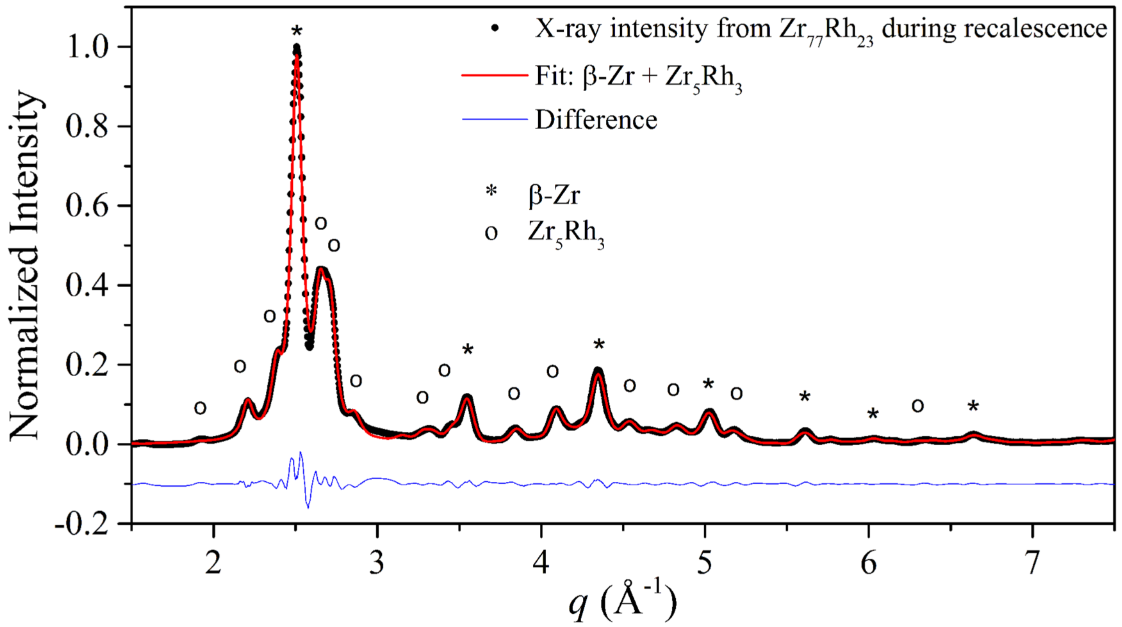

FIG. 11. Identification of a phase mixture of β-Zr (asterisks) and Zr_5Rh_3 (open circles) crystalline phases that crystallized from a supercooled (more than 200 °C) $Zr_{77}Rh_{23}$ liquid.

among the remaining dominant structures. The high-frequency of these 12 coordinated structures likely aids in the formation of the quasicrystal phase upon cooling.

E. Crystal identification

Although complete chemical information cannot be extracted for $Zr_{77}Rh_{23}$, the similar CNs with those for $Zr_{80}Pt_{20}$ and the similarities of $S_{BT}(q)$ and $g_{BT}(r)$ suggest that these two liquids are at least topologically similar. While there appears to be a much higher correlation between topological and chemical ordering in $Zr_{77}Rh_{23}$, the stability of the $\langle 0\ 2\ 8\ 1\ 0\rangle$ cluster makes it likely that it is also prevalent in $Zr_{77}Rh_{23}$. Since this polyhedron is also found in the Zr_5Pt_3 crystal phase (Mn_5Si_3-type, space group $P6_3/mcm$) [66,67], it would seem that a similar phase might form in $Zr_{77}Rh_{23}$. Although this phase has not been observed in studies of the Zr-Rh and Zr-Pd equilibrium phase diagrams [68,69], it does form in Zr-Ir alloys (Zr_5Ir_3) [70]. Given this, an equivalent Mn_5Si_3-type phase is likely close to equilibrium in all of the Zr-NM alloys and may form as a metastable product during crystallization. This appears to be the case for Zr-Rh. Shown in Fig. 11 are Rietveld refinements (using GSAS II [71]) to x-ray data taken during the recalescence of liquid $Zr_{77}Rh_{23}$ (with more than 200 °C supercooling). These indicate the presence of two phases, β-Zr and a hexagonal Mn_5Si_3-type phase. The most intense peaks are from β-Zr (*), and all remaining peaks belong to the proposed Zr_5Rh_3 phase (○). Starting with the lattice parameters for Zr_5Pt_3 ($a = 8.201$ Å and $c = 5.405$ Å) [66,67], the converged fits gave $a = 7.95$ Å and $c = 5.6$ Å for Zr_5Rh_3, closer to those found for Zr_5Ir_3 ($a = 8.025$ Å and $c = 5.488$ Å) [70]. The differences in the lattice parameters may arise from the nonequilibrium conditions during the nucleation and growth of the metastable phase, likely arising from chemical substitutions within the lattice that distorts the average atomic distances.

IV. CONCLUSION

In summary, neutron scattering results of liquid and supercooled $Zr_{80}Pt_{20}$ and $Zr_{77}Rh_{23}$, made using a new electrostatic levitation facility [38], are reported. By combining these data with high-energy x-ray scattering studies of these liquids at equivalent temperatures, it is possible to extract topological and chemical ordering information. The x-ray and neutron structure factors were combined with $g_{ZrZr}(r)$ and $g_{ZrPt}(r)$ from MD to obtain the partials and atomic structure for liquid $Zr_{80}Pt_{20}$ using the constrained RMC method. A prepeak in the scattering data for $Zr_{80}Pt_{20}$ is consistent with medium-range ordering, arising from extended Pt-Pt correlations. Bhatia-Thornton partials for $Zr_{77}Rh_{23}$ were obtained by ignoring the CC contribution (between 1 and 2% of the total) and calculating the NN and NC partials using x-ray and neutron scattering measurements. For $Zr_{80}Pt_{20}$, they were calculated directly from the FZ partials determined from CRMC. From this, the two liquids were found to be topologically similar. The smaller cross-partial S_{NC} for $Zr_{80}Pt_{20}$ suggests that the charge transfer between Zr and Pt induces chemical order and, at the same time, reduces the atomic size difference. Combined with the lack of a prepeak in the diffraction data, it is suggested that there is strong Rh-Rh chemical SRO, but weaker size-induced MRO. The Voronoi results for the Zr-Pt liquid showed a mixture of ordered and distorted FK polyhedra, as well as a dominant Pt-centered $\langle 0\ 2\ 8\ 1\ 0\rangle$ cluster, a structure also found around the Pt atoms in the Zr_5Pt_3 equilibrium crystal phase. A similar metastable phase was found to crystallize from a deeply supercooled (>200 °C) $Zr_{77}Rh_{23}$ liquid; this phase has not previously been reported, to our knowledge, in this binary alloy.

In addition to identifying some features of Zr-NM liquids, these results, based on multiple types of scattering experiments and combined with MD simulations, demonstrate the ability to study the chemical and topological ordering as a function of supercooling in containerless-processed metallic liquids. This information is critically important in developing a better understanding of the relation between structure and properties, crystal nucleation, potential liquid/liquid phase transitions, and ultimately glass formation.

ACKNOWLEDGMENTS

The authors thank Doug Robinson for his assistance with the high-energy x-ray diffraction studies at the APS, Kevin Derendorf for his contributions to the design and construction of the NESL, Ken Herwig for logistics and travel support, Vy Tran and Ryan Soklaski for the use of their Voronoi code and useful discussions, and Zackary Markow for useful discussions. The work at Washington University in Saint Louis was partially supported by the National Science Foundation under Grant No. DMR-12-06707 and the National Aeronautics and Space Administration (NASA) under Grant No. NNX10AU19G. The work at Iowa State University was supported by the National Science Foundation under Grant No. DMR-1308099. T. Egami acknowledges the support from the US Department of Energy, Office of Science, Basic Energy Sciences, Materials Science and Engineering Division. The synchrotron measurements were made on the Sector 6 beamline at the APS. Use of the APS is supported by the US Department of Energy, Basic Energy Science, Office of Science, under Contract No. DE-AC02-06CH11357. This research at the SNS was sponsored by the U.S. Department of Energy, Office of Basic Energy Sciences, Scientific User Facilities Division. Any opinions, findings, and conclusions or recommendations expressed in this material are those of the author(s) and do not necessarily reflect the views of the National Science Foundation or of NASA.

---

[1] N. A. Mauro, M. E. Blodgett, M. L. Johnson, A. J. Vogt, and K. F. Kelton, Nat. Comm. **5**, 4616 (2014).

[2] N. A. Mauro, A. J. Vogt, M. L. Johnson, J. C. Bendert, R. Soklaski, L. Yang, and K. F. Kelton, Acta Mater. **61**, 7411 (2013).

[3] S. Klein, D. Holland-Moritz, D. M. Herlach, N. A. Mauro, and K. F. Kelton, Europhys. Lett. **102**, 36001 (2013).

[4] N. A. Mauro and K. F. Kelton, J. Non-Cryst. Solids **358**, 3057 (2012).

[5] N. A. Mauro, W. Fu, J. C. Bendert, Y. Q. Cheng, E. Ma, and K. F. Kelton, J. Chem. Phys. **137**, 044501 (2012).
[6] V. Wessels, A. K. Gangopadhyay, K. K. Sahu, R. W. Hyers, S. M. Canepari, J. R. Rogers, M. J. Kramer, A. I. Goldman, D. Robinson, J. W. Lee, J. R. Morris, and K. F. Kelton, Phys. Rev. B **83**, 094116 (2011).
[7] G. W. Lee, A. K. Gangopadhyay, R. W. Hyers, T. J. Rathz, J. R. Rogers, D. S. Robinson, A. I. Goldman, and K. F. Kelton, Phys. Rev. B **77**, 184102 (2008).
[8] D. Holland-Moritz, F. Yang, J. Gegner, T. Hansen, M. D. Ruiz-Martín, and A. Meyer, J. Appl. Phys. **115**, 203509 (2014).
[9] T. Kordel, D. Holland-Moritz, F. Yang, J. Peters, T. Unruh, T. Hansen, and A. Meyer, Phys. Rev. B **83**, 104205 (2011).
[10] D. Holland-Moritz, O. Heinen, R. Bellissent, and T. Schenk, Mater. Sci. Eng. A **449**, 42 (2007).
[11] T. Schenk, D. Holland-Moritz, V. Simonet, R. Bellissent, and D. Herlach, Phys. Rev. Lett. **89**, 075507 (2002).
[12] L. Huang, C. Z. Wang, S. G. Hao, M. J. Kramer, and K. M. Ho, Phys. Rev. B **81**, 014108 (2010).
[13] R. Soklaski, Z. Nussinov, Z. Markow, K. F. Kelton, and L. Yang, Phys. Rev. B **87**, 184203 (2013).
[14] R. Soklaski, V. Tran, Z. Nussinov, K. F. Kelton, and L. Yang, arXiv:1502.01739.
[15] K. F. Kelton, G. W. Lee, A. K. Gangopadhyay, R. W. Hyers, T. J. Rathz, J. R. Rogers, M. B. Robinson, and D. S. Robinson, Phys. Rev. Lett. **90**, 195504 (2003).
[16] F. Frank, Proc. R. Soc. London, Ser. A **215**, 43 (1952).
[17] P. Ganesh and M. Widom, Phys. Rev. B **74**, 134205 (2006).
[18] P. J. Steinhardt, D. R. Nelson, and M. Ronchetti, Phys. Rev. Lett. **47**, 1297 (1981).
[19] T. Tomida and T. Egami, Phys. Rev. B **52**, 3290 (1995).
[20] G. W. Lee, A. K. Gangopadhyay, K. F. Kelton, R. W. Hyers, T. J. Rathz, J. R. Rogers, and D. S. Robinson, Phys. Rev. Lett. **93**, 037802 (2004).
[21] T. H. Kim and K. F. Kelton, J. Chem. Phys. **126**, 054513 (2007).
[22] J. Saida, M. Matsushita, and A. Inoue, Appl. Phys. Lett. **77**, 73 (2000).
[23] B. S. Murty, D. H. Ping, and K. Hono, Appl. Phys. Lett. **77**, 1102 (2000).
[24] B. S. Murty, D. H. Ping, M. Ohnuma, and K. Hono, Acta Mater. **49**, 3453 (2001).
[25] D. J. Sordelet, X. Y. Yang, E. A. Rozhkova, M. F. Besser, and M. J. Kramer, Appl. Phys. Lett. **83**, 69 (2003).
[26] D. J. Sordelet, E. Rozhkova, M. F. Besser, and M. J. Kramer, J. Non-Cryst. Solids **334**, 263 (2004).
[27] J. Saida, M. Matsushita, and A. Inoue, J. Appl. Phys. **90**, 4717 (2001).
[28] D. J. Sordelet, R. T. Ott, M. Z. Li, S. Y. Wang, C. Z. Wang, M. F. Besser, A. C. Y. Liu, and M. J. Kramer, Metall. Mater. Trans. A **39**, 1908 (2007).
[29] M. H. Lee, X. Yang, M. J. Kramer, and D. J. Sordelet, Philos. Mag. **86**, 443 (2006).
[30] C. Li, L. Wang, and A. Inoue, J. Phys.: Condens. Matter **13**, L803 (2001).
[31] S. Wang, C. Wang, M. Li, L. Huang, R. Ott, M. Kramer, D. Sordelet, and K. Ho, Phys. Rev. B **78**, 184204 (2008).
[32] M. H. Lee, R. T. Ott, M. F. Besser, M. J. Kramer, and D. J. Sordelet, Scr. Mater. **55**, 505 (2006).
[33] N. A. Mauro, V. Wessels, J. C. Bendert, S. Klein, A. K. Gangopadhyay, M. J. Kramer, S. G. Hao, G. E. Rustan, A. Kreyssig, A. I. Goldman, and K. F. Kelton, Phys. Rev. B **83**, 184109 (2011).
[34] T. E. Faber and J. M. Ziman, Philos. Mag. **11**, 153 (1965).
[35] A. K. Gangopadhyay, G. W. Lee, K. F. Kelton, J. R. Rogers, A. I. Goldman, D. S. Robinson, T. J. Rathz, and R. W. Hyers, Rev. Sci. Instrum. **76**, 073901 (2005).
[36] N. A. Mauro and K. F. Kelton, Rev. Sci. Instrum. **82**, 035114 (2011).
[37] J. Neuefeind, M. Feygenson, J. Carruth, R. Hoffmann, and K. K. Chipley, Nucl. Instrum. Methods Phys. Res., Sect. B **287**, 68 (2012).
[38] N. A. Mauro, A. J. Vogt, K. S. Derendorf, M. L. Johnson, G. E. Rustan, D. G. Quirinale, A. Kreyssig, K. A. Lokshin, J. C. Neuefeind, Ke An, Xun-Li Wang, A. I. Goldman, T. Egami, and K. F. Kelton, Rev. Sci. Instrum. **87**, 013904 (2016).
[39] K. Derendorf, Ph.D. dissertation, Washington University in St. Louis, 2013.
[40] A. J. Vogt, Ph.D. dissertation, Washington University in St. Louis, 2014.
[41] J. C. Bendert, C. E. Pueblo, S. Veligati, N. A. Mauro, and K. F. Kelton, Int. J. Thermophys. **35**, 1687 (2014).
[42] R. C. Bradshaw, D. P. Schmidt, J. R. Rogers, K. F. Kelton, and R. W. Hyers, Rev. Sci. Instrum. **76**, 125108 (2005).
[43] S. K. Chung, D. B. Thiessen, and W.-K. Rhim, Rev. Sci. Instrum. **67**, 3175 (1996).
[44] J. C. Bendert and K. F. Kelton, Int. J. Thermophys. **35**, 1677 (2014).
[45] J. C. Bendert, N. A. Mauro, and K. F. Kelton, J. Appl. Crystallogr. **46**, 999 (2013).
[46] K. Page, C. E. White, E. G. Estell, R. B. Neder, A. Llobet, and T. Proffen, J. Appl. Crystallogr. **44**, 532 (2011).
[47] P. F. Peterson, E. S. Božin, T. Proffen, and S. J. L. Billinge, J. Appl. Crystallogr. **36**, 53 (2003).
[48] R. L. McGreevy, J. Phys.: Condens. Matter **13**, R877 (2001).
[49] O. Gereben, P. Jovari, L. Temleitner, and L. G. Pusztai, J. Optoelectron. Adv. Mater. **9**, 3021 (2007).
[50] J. L. Finney, Proc. R. Soc. London, Ser. A **319**, 479 (1970).
[51] J. L. Finney, Nature (London) **266**, 309 (1977).
[52] C. H. Rycroft, Chaos **19**, 041111 (2009).
[53] J. Park and Y. Shibutani, Intermetallics **23**, 91 (2012).
[54] W. F. Gale and T. C. Totemeier, *Smithells Metals Reference Book* (8th ed.) (Elsevier, Oxford, 2004).
[55] J. Saida, K. Itoh, S. Sato, M. Imafuku, T. Sanada, and A. Inoue, J. Phys.: Condens. Matter **21**, 375104 (2009).
[56] H. W. Sheng, W. K. Luo, F. M. Alamgir, J. M. Bai, and E. Ma, Nature (London) **439**, 419 (2006).
[57] C. N. J. Wagner, J. Non-Cryst. Solids **76**, 29 (1985).
[58] N. Mattern, A. Schöps, U. Kühn, J. Acker, O. Khvostikova, and J. Eckert, J. Non-Cryst. Solids **354**, 1054 (2008).
[59] N. Mattern, P. Jóvári, I. Kaban, S. Gruner, A. Elsner, V. Kokotin, H. Franz, B. Beuneu, and J. Eckert, J. Alloys Compd. **485**, 163 (2009).
[60] J. Saida, K. Itoh, T. Sanada, S. Sato, M. Imafuku, M. Ohnuma, and A. Inoue, J. Alloys Compd. **509S**, S27 (2011).
[61] A. B. Bhatia and D. E. Thornton, Phys. Rev. B **2**, 3004 (1970).
[62] D. Holland-Moritz, F. Yang, T. Kordel, S. Klein, F. Kargl, J. Gegner, T. Hansen, J. Bednarcik, I. Kaban, O. Shuleshova, N. Mattern, and A. Meyer, Europhys. Lett. **100**, 56002 (2012).
[63] F. C. Frank and J. S. Kasper, Acta Crystallogr. **12**, 483 (1959).

[64] E. Matsubara, T. Nakamura, M. Sakurai, M. Imafuku, S. Sato, J. Saida, and A. Inoue, MRS Proceedings **644**, L1.1.1 (2000).

[65] See Supplemental Material at http://link.aps.org/supplemental/10.1103/PhysRevB.93.054203 for temperature dependent indices.

[66] P. Villars, *Material Phases Data System (MPDS)* (SpringerMaterials, CH-6354 Vitznau, Switzerland, 2014).

[67] T. K. Biswas and K. Schubert, Z. Metallkd. **58**, 558 (1967).

[68] D. Arias and J. P. Abriata, J. Phase Equilib. **14**, 110 (1993).

[69] R. M. Waterstrat, A. Shapiro, and A. Jeremie, J. Alloys Compd. **290**, 63 (1999).

[70] H. Okamoto, J. Phase Equilib. **13**, 653 (1992).

[71] B. H. Toby and R. B. Von Dreele, J. Appl. Crystallogr. **46**, 544 (2013).